Fuel cell electrocatalsis : oxygen reduction on Pt-based nanoparticle catalysts

Vliet, D.F. van der

Chapter 7

Multimetallic Nanotubes as Catalysts for the Oxygen Reduction Reaction

The most challenging problems in fuel cell technology are the insufficient activity of the catalyst for the cathodic oxygen reduction reaction (ORR), catalyst degradation, and carbon support corrosion. To improve the former, and avoid the latter, carbon-free multimetallic nanotube catalysts that can attain superior rates of activity for the ORR have been synthesized. The composition and surface morphology of the multimetallic nanotubes have been tuned to improve their affinity for the ORR. The level of activity for the fuel cell cathodic reaction established on the multimetallic nanotube catalyst exceeds the highest value reported for bulk polycrystalline Pt bimetallic alloys, and it is 60-fold more active than the current state-of-the-art Pt/C nanoscale catalyst.

7.1 Introduction

Hydrogen fuel cell research is a major effort over the last few decades with many companies working to make fuel cell operated devices and vehicles available to the general public. A major challenge lies in optimizing the cathode side of the fuel cell. Whereas the hydrogen oxidation reaction (HOR) on the anode side is easily catalyzed and well understood, the oxygen reduction (ORR) on the cathode side is trickier. The reversible potential for the ORR at 1.23 V vs RHE is not reached in real fuel cells due to the inactivity of current catalysts, leading to losses of potential of more than 400 mV. Due to this lower operating potential, the thermal efficiency drops well below the theoretical value of 83% at the reversible potential. It is therefore of importance to increase the activity of ORR catalyst to reduce this overpotential and increase fuel cell efficiency. [1-13].

Most of the research centers around platinum, as it is the best monometallic ORR catalyst. There is, however, the scarceness and cost of Pt to consider as well. As the implementation of fuel cells worldwide would require a significant amount of catalyst, this would put an enormous strain on the Pt stock, as well as raise the price of a fuel cell significantly. With the current state-of-the-art catalyst, an approximate five fold reduction in Pt content is necessary to meet requirements in cost for large scale automotive applications [1]. This has fueled the interest to search for relatively cheaper non-precious metals as catalysts [14-19] Moreover, multi-metallic alloys have made significant impact in fuel cell catalyst design by decreasing the amount of platinum while improving activity and durability [20], and are thus the focus of much research, both on bulk electrodes [20-32], and in nanoscale catalysts. [33-37] Rather than a trial and error approach in synthesizing these alloys, we have relied in previous work on well-defined, extended surfaces. [20-22] Pt_3Ni and Pt_3Co alloy catalysts are the most active catalysts for the ORR to date [21], with Pt_3Ni (111) skin electrodes being the most active of all [20]. Therefore nanoscale systems based on these metals were synthesized by 3M. Rather than using PtNi nanoparticles on Carbon [31, 38, 39], a Pt-alloy nanostructured thin film (NSTF) catalyst, which required no high-surface-area carbon support, was prepared by 3M, therby eliminating carbon support corrosion. This NSTF catalyst is prepared by sputtering metal layers on a polymer substrate and is shown to have increased activity and stability compared to traditional carbon-supported nanoparticles. [40, 45-47]

7.2 Experimental

Consecutive layers of platinum and nickel were sputtered on a crystallized organic pigment (*N*,*N*-di(3,5-xylyl)perylene-3,4:9,10bis(dicarboximide), in short: perylene red) in Ultra High Vacuum (UHV). [45, 46] The sputtering covered each of the perylene red whiskers with a thin metallic film. The platinum and nickel were sputtered on the substrate one after the other; the deposition resulting in a metal-covered, whiskered polymer, see figure 7.1. Both the monometallic Pt and the PtNi alloy catalyst were created by this method.

The whiskers thus created were gently brushed off the perylene red and collected, creating in essence a catalyst powder. The inside of the whiskers still contained residue of the polymer and in some places several whiskers were clumped together. However, the resulting powder of these whiskers allowed suspending them in water. The mass of the catalyst is determined by weighing on a microbalance before transferring to a clean container and the desired amount of pure water is added. This allows for a relatively accurate determination of the amount of catalyst per unit volume in the suspension. The suspension is then sonicated for at least 45 minutes before depositing a known amount on a polished glassy carbon disk, so that the disk will contain the desired loading of Pt. The pipetted drop is then let to dry in a light argon stream at about 50°C. When the drop has dried, the catalyst is firmly attached to the GC disk, without the need for nafion. Before immersion in the cell at potential control, the surface of the disk was gently washed with a small flow of ultrapure water to dislodge any loosely bound particles, and to assure that the layer was stable.

The nanotubes were generated by thermally annealing the brushed-off whiskers in a tube furnace in a hydrogen atmosphere, as depicted in schematic form in figure 7.2. About 1.5 mg catalyst was deposited on a small tray in the middle of a quartz glass tube in a furnace (Carbolite MTF 10/15/160) at room temperature. For 15 minutes research grade argon gas was blown through the tube to purge all oxygen out, followed by flowing research grade hydrogen to create a pure hydrogen atmosphere. After the pure hydrogen atmosphere is achieved, the furnace is set to 100 °C. The furnace is kept at 100 °C for 30 minutes to make sure all possible water evaporates from the sample. Consequently the temperature is increased in 100 °C increments every 15 minutes until the temperature of 400°C is reached. The furnace is then kept at 400 °C for 4 hours, after which heating is shut off and the catalyst slowly cooled to < 90°C at which temperature the flow of gas in the cell is switched

to a mixture of 5% hydrogen in Argon. The catalyst is then let to cool overnight in this gas flow. When preparing the nanotube electrode, the catalyst powder from the furnace was treated identical to the whiskers described above.
An Autolab PGSTAT 30 with FI20, ECD, ADC and SCAN GEN modules was used for the electrochemical measurements. Perchloric acid of 0.1M, created by diluting concentrated $HClO_4$ (70%, JT Baker ULTREX II Ultrapure Reagent) with MilliQ water, was in all cases the electrolyte. All gases were research grade (5N5+). A silver-silver chloride reference electrode was used. However, all potentials referred to in this paper are converted to the pH independent RHE scale. All experiments were repeated a substantial amount of times (at least 4 times each) to confirm reproducibility, and to improve accuracy in the determination of kinetic activities.
A measured ORR curve consist of a kinetic contribution and a diffusion contribution according to the relation $I_{ORR}^{-1} = I_{kinetic}^{-1} + I_{diffusion}^{-1}$. The kinetic current densities ($i_{kinetic} = I_{kinetic}$ / Active Surface Area) were deduced from the measured ORR curve by using this relation. The active surface area of the nanocatalysts was determined by integrating the H_{upd} part of the CV and correcting for the double layer charge as described in [37].

7.3 Results

7.3.1 Catalyst preparation and characterization

The schematic in the middle of figure 7.1 shows the step by step deposition of the catalyst onto the polymer film, and the SEM images (figure 7.1 A-D) show the morphology of the nanostructured thin film (NSTF). Figure 7.1A shows the extended surface morphology of the particles in the NSTF. The ordering of these particles on this support is very random and disoriented. Figure 7.1B shows a close up of a broken particle from which is clear that if the support is removed, hollow particles will emerge. The whiskers have a very rough outer surface with smaller individual whiskers on top of the large ones. Images D and E indicate that the outside of the particles is very rough and full of low-coordinated Pt atoms. However, Gancs *et al.* [40] recently reported that these small side whiskers have mainly (111) facets with a small amount of (100) facets. Figure 7.1E shows a TEM image which clearly shows a relatively thin particle with surface stumps. To analyze this catalyst in a controlled way and compare it to state of the art Pt/C

catalyst we opted to use the Rotating Disk Electrode (RDE) method. (see [41] and Methods section) The increased specific activity for monometallic Pt NSTF catalysts versus Pt/C has been reported before. [40]

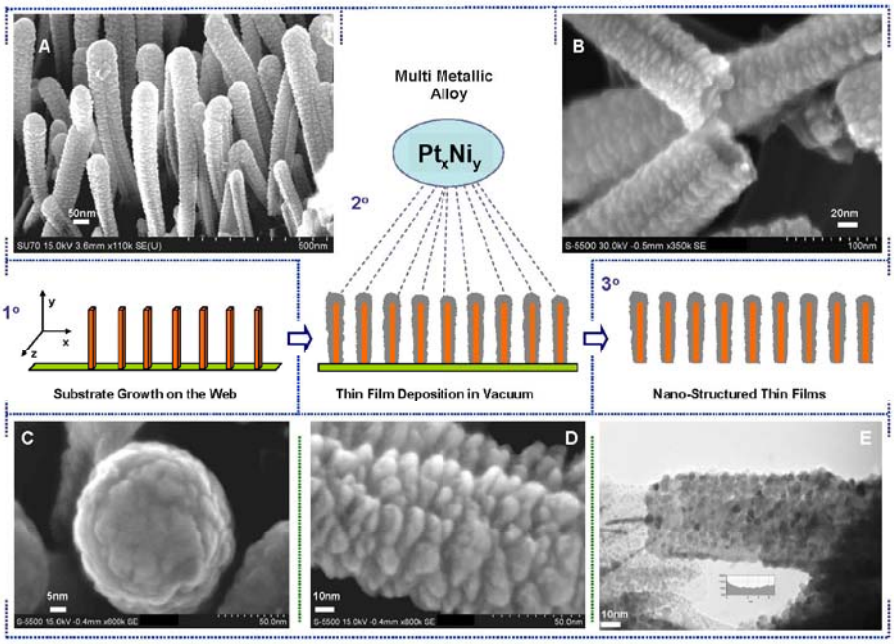

Figure 7.1, SEM images of the NSTF catalyst. Part A shows the macroscopic structure of the separate particles on the support. B shows a broken particle. C and D are close ups, with E a TEM image of this catalyst. Inset in the middle shows the production process.

However, a second approach to prepare the particles for RDE measurements was also performed. In an effort to clean the metallic particles from its supporting polymer, the catalyst was annealed prior to deposition on the glassy carbon (GC) disk; TEM images A through C show that in time the polymer substrate is disappearing and the particles become hollow. More information on the annealing preocedure can be found in the section 7.2. The time it takes to remove most of the perylene red is estimated to be about an hour from observations during the experiment with variable annealing times; details can be found in section 7.5. Figure 7.2A' through C' show that in time the surface structure changes as well with annealing; the low coordinated surface Pt disappear and a more smooth hollow nanotube emerges. The optimal time of annealing at 400 °C in a pure H_2 flow was deduced to be four hours. (see section 7.5)

The smoothening of the particles into nanotubes is expected to lower the surface area, which it does, but not by a large margin. The decrease in total electrochemical

surface area per μg_{Pt} after annealing is 10%, from an average 9.8 m^2 g_{Pt}^{-1} for the PtNi NSTF to an average 8.7 m^2 g_{Pt}^{-1} for the nanotubes. The active surface area was deduced from the charge of adsorbed hydrogen, as explained in [37]. The reason for this relatively small decrease is that a large portion of the surface on the inside was blocked by the polymer in the NSTF, and has been opened up after annealing the polymer, counterbalancing the loss in surface area through smoothening of the particles. As we will show below, the decrease in surface area is compensated by the increase in specific activity, so that even the mass activity has improved significantly.

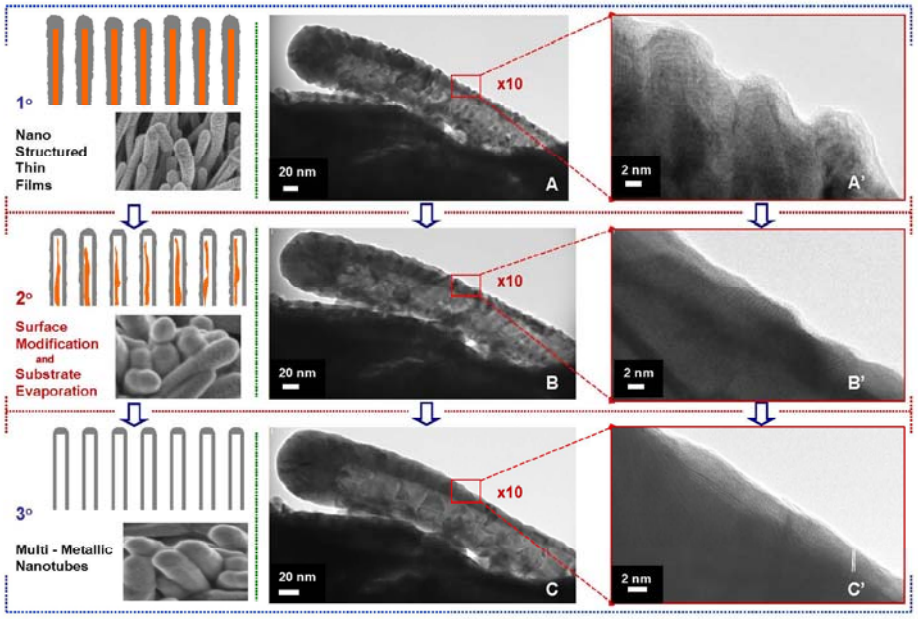

Figure 7.2. Schematic of the process of annealing the NSTF. TEM images A-C show the progressive substrate evaporation, while images A'-C' show the surface modification.

The XRD experiments shown in figure 7.3, show that during annealing there is a small angle shift, due to the lowered lattice constant, which points to further alloying of the catalyst with Pt atoms being replaced by Ni in the crystal lattice. Furthermore, the grain size of the (111) facets increase as is evident from the increased sharpness of the (111) peak in the XRD pattern. Finally the ratio between the (111) and (200) orientations has increased from 1 to 1.2, reinforcing the conclusion that with annealing the (111) facets on the nanotubes are improved and extended.

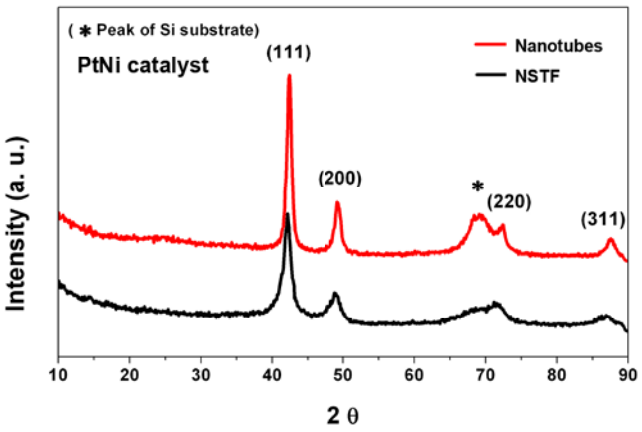

Figure 7.3. XRD analysis of PtNi nanotubes compared to its NSTF precursor. A small angle shift is visible after creating the rods, as well as grain size increase and ratio change between (111) and (200).

7.3.2 Electrochemical characterization

The PtNi NSTF catalyst exhibits very similar behavior to its monometallic counterpart in cyclic voltammetry, as shown in figure 7.4A. The region at low potentials, where hydrogen adsorb (< 0.4V in for the PtNi NSTF catalyst), is called the H_{upd} region. Small, features are visible in the H_{upd} region for PtNi NSTF (green curve) at about 0.1V,presumably due to (110)-sites [48, 49], similar to Pt NSTF (black curve). Oxide formation (at potentials > 0.7V; the surface oxide region) has a 50 mV higher onset on PtNi, compared to monometallic Pt, which is a first indication of the higher activity for the ORR, as surface oxides are the blocking species for the ORR on the catalyst surface [21]. However, the amount of surface oxides seems to be significantly larger than on Pt, as can be deduced from the charge under the CV in the surface oxide region. A possible explanation is that nickel readily oxidizes, but adsorbs no hydrogen in the H_{upd} region of a CV, leading to the observed discrepancy between the oxide region of monometallic Pt and the PtNi alloy.

The PtNi nanotubes behave very similar to the PtNi NSTF in this oxide region, the only difference being a slight delay in OH adsorption on the nanotubes compared to the NSTF. The H_{upd} part of the curve, however, is quite different. The Pt (111) CV is shown in the graph to point out the similarities between the single crystal and the PtNi nanotubes in the H_{upd} region. The flat feature for PtNi nanotubes may indicate that the surface of the particles has a large contribution of (111) facets compared to

(110) and (100). In the oxide region, however, the nanotubes' onset for the adsorption of oxide containing species is delayed with about 160 mV compared to Pt (111).

7.3.3 ORR

The ORR polarization curves are shown in figure 7.4B. All catalysts reach the expected theoretical diffusion limiting current on a 6 mm disk with a rotation of 1600 rpm. Kinetic current densities for the ORR are shown in figure 7.4C as Tafel plots. (For the determination of the kinetic current densities from the ORR curves, see section 7.2) In this figure, the order of kinetic currents becomes apparent, with Pt/C being the least active surface per unit of surface area, followed by Pt NSTF. A significant increase in activity is observed for the nanotubes as compared to the PtNi NSTF, and will be discussed below. The Tafel slopes can be deduced from this graph and follow an interesting trend: the higher the activity for oxygen reduction, the lower the Tafel slope. This means that the steepness of the curve, which is the increase in reaction velocity, is increased more than the onset of the ORR. Values for the Tafel slope range from 60 mV per decade and 70 mV dec^{-1} for Pt NSTF and polycrystalline Pt respectively, to 41 mV dec^{-1} for PtNi NSTF and nanotubes. Tafel slopes are often used to deduce information on reaction pathways, and values of 40 and 60 mV dec^{-1} point to different rate determining steps. The value of 60 mV dec^{-1} is typical for an electrochemical equilibrium, followed by a rate determining chemical step, whereas 40 mV dec^{-1} points to an electrochemical equilibrium, followed by an electrochemical rate determining step [42]. If in this case the Tafel slope holds the same information is debatable, as in our experiments on different NSTF catalysts a whole range of slopes from 40 to 60 mV dec^{-1} were found, and the mechanism of oxygen reduction is not expected to differ. These values are significantly lower from those obtained in the literature before (*e.g.* [21, 43]), which can be explained by the fact that those particular measurements did not correct for solution resistance. The importance of correcting for solution resistance is illustrated in Chapter 2 of this thesis.

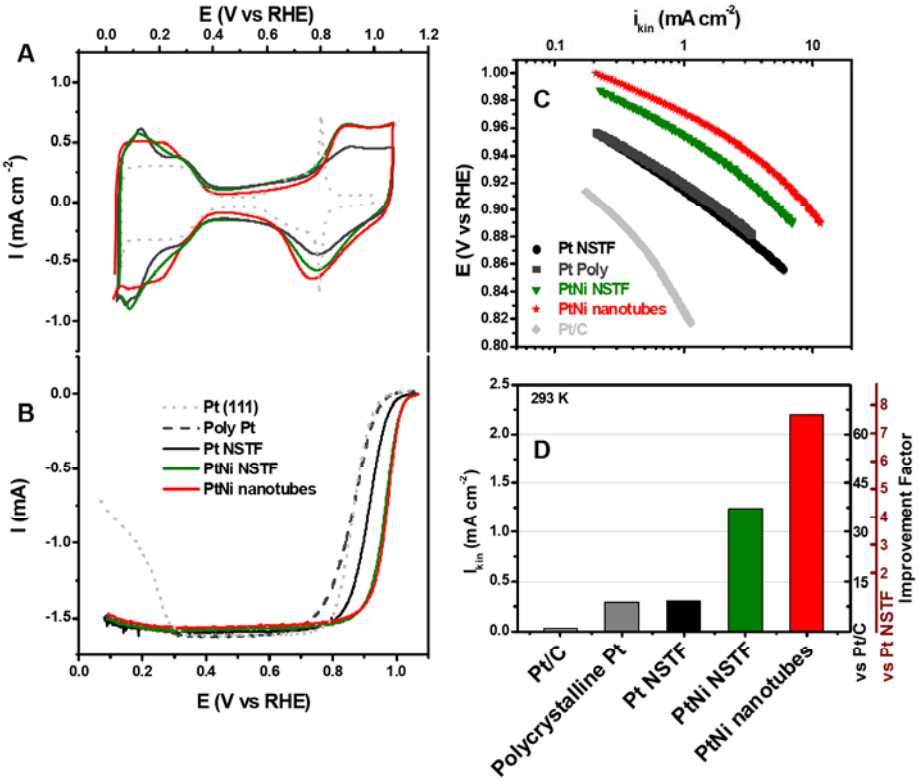

Figure 7.4. Cyclic voltammetry and Oxygen Reduction reaction on the NSTF catalysts. CVs are shown in A, measured with 50 mV $^{S-}$1 in 0.1M HClO4. The full ORR curves shown in B, measured in 0.1M $HClO_4$ with 20 mV $s^{-1.}$ The tafel slopes for the curves in B are shown in C. The bar graphs in D show the kinetic current and the improvement factor versus Pt (both carbon supported and NSTF). Values for Pt_3Ni skeleton and skin structures obtained from [19].

Concerning the activity for the ORR, there is a significant effect of both alloying and annealing. Similar as reported in [21], the bimetallic PtNi catalyst has a higher kinetic activity than platinum. In this case the PtNi whiskers are most properly compared to their own monometallic counterpart (Pt NSTF). The comparison is made by measuring the kinetic current density at 0.95V vs RHE for the catalysts. A lower potential of 0.9V or even 0.85V as has been used in the past [1, 20, 27, 43] is less accurate as the ORR on the alloy catalyst particles is so active at these potentials, that the current is strongly controlled by diffusion, see figure 7.4B. At 0.95V vs. RHE the kinetic current measured for the PtNi NSTF catalyst is 4.1 times higher than that for the monometallic Pt. The activity for the PtNi NSTF is even higher than the bulk Pt_3Ni alloy. When we subsequently anneal the PtNi catalyst

and create the nanorods, the activity increases to an improvement factor of 7.3 over Pt NSTF. This trend is similar to observed before [27], where annealed Pt_3Ni formed the "skin" Pt_3Ni structure, which was found to be more active for the ORR than the non-annealed "skeleton" structure. The NSTF and the nanotubes are about twice as active as these bulk Pt_3Ni alloys. When we compare the activity of the PtNi nanotubes to the value reported for the industry standard high-surface area catalyst [1], there is an improvement factor of over 60 versus Pt/C. The PtNi nanotube activity also surpasses bulk polycrystalline Pt, which is 10 times more active than Pt/C.

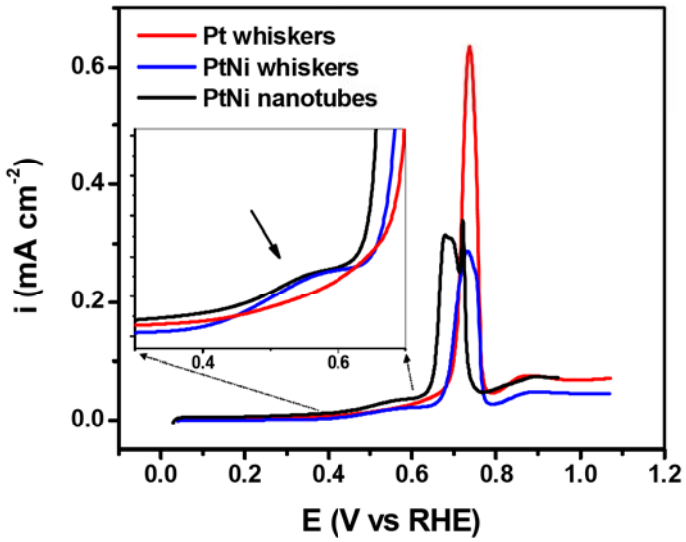

Figure 7.5. CO stripping on PtNi NSTF and nanotubes. Scan rate 50 mV s^{-1}. Inset shows an enlarged portion of the curve with an emphasis on a pre-oxidation peak.

At elevated temperatures of 60°C the improvement factors show similar trends, though the magnitudes differ. Monometallic Pt becomes more active at this temperature, whereas the PtNi catalyst does not. The improvement factor of the PtNi whiskers versus Pt at 60°C is 2.8. Nanotubes are about 1.3 times more active than PtNi whiskers at 60°C, and an improvement factor of 4.3 versus monometallic Pt NSTF is obtained. The improvement factor versus polycrystalline-Pt is still more than 3, which indicates that at 60 °C, the catalyst is still more active than bulk polycrystalline Pt-skin and skeleton type alloys. [27] One possible reason for the absence of activation of the PtNi catalyst at higher temperatures is the higher contamination level in a heated electrochemical cell. The more active catalyst sites

on this particular catalyst compared to monometallic Pt will be more sensitive to the same levels of small organic contaminations present in the cell.

To confirm that oxide containing species indeed adsorb at lower potentials on the PtNi nanotubes and to measure the true double layer charge for the electrochemical surface area determination as explained in [37], CO stripping experiments were performed. These are shown in figure 7.5 and give a CO coverage of 0.88 on the PtNi whiskers by comparing the charge of CO stripping with the charge of H_{upd}. This coverage is comparable to experiments performed on the monometallic Pt whiskers, where coverage was found to be 0.85. The result of CO stripping on the PtNi nanotubes is identical to the whiskers, with a coverage of 0.88, indicating that the surface composition of both catalysts must be similar. Furthermore, the CO stripping curves corroborate our conclusion that the nanotubes have a lower affinity for adsorption of oxide species, and that there are fewer low-coordinated Pt atoms on the surface. It has been shown before that low coordinated "defect" sites on well defined surfaces are the most active sites for CO oxidation [44]. In figure 7.5, a pre-peak can be seen for the NSTF catalysts, indicative of ample low-coordinated Pt sites on the surface, but no such peak is observed for the nanotubes. Furthermore, CO stripping from the surface proper starts at higher potentials for tubes, compared to the whiskers, while at monometallic Pt CO oxidation starts at an even lower potential. The combination of the higher onset potential for CO oxidation, together with the absence of a pre-peak is further evidence for the smoother defect-poor surface of the nanotubes.

A defect-poor surface does have the added disadvantage of a lower active surface area per unit of weight of Pt. As mentioned earlier, the PtNi nanotubes have a significant 10% decrease in surface area compared to the NSTF alloy. This means that the ratio between mass activities of the nanotubes versus the NSTF catalyst will diminishe slightly compared to ratio of the kinetic current densities. However, as is shown in figure 7.6, the nanotubes are still more active than the NSTF. And more importantly: both catalysts are more active than the carbon supported catalyst by a factor of 4 (whiskers) and 7 (nanotubes), despite the 25 times higher surface area per g_{Pt} for this highly dispersed catalyst [1].

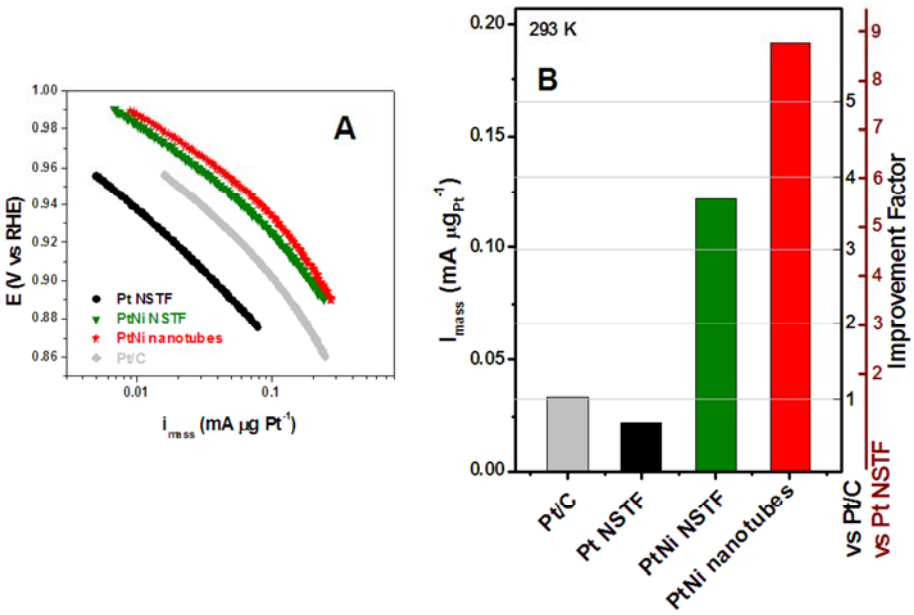

Figure 7.6. ORR mass activities of the nanocatalysts.

7.4 Conclusion

In summary, a novel method of nanocatalyst preparation has been reported. PtNi nanorods were created specifically tailored to inhibit surface oxidation, thereby activating the oxygen reduction reaction. CO stripping curves and X-ray diffraction patterns confirm the formation of a smoother, less defected surface after annealing of the PtNi NSTF catalyst to create PtNi nanotubes.

The highest kinetic activities ever measured for the ORR for nanocatalysts have been reported in this paper. Improvement factors of 7.5 versus polycrystalline Pt, 7.3 over monometallic Pt NSTF and more than 60 versus Pt/C were measured at room temperature. Even at 60°C the activities for PtNi nanorods exceed those of very active Pt-skin type polycrystalline alloys, with an increase in activity of 40 versus Pt/C and 4.5 versus polycrystalline Pt. More important is perhaps the significant increase in mass activity versus highly dispersed Pt nanoparticles on carbon. The 5.8 fold increase in activity versus Pt/C mass activity values at 20°C and 3.4 fold at 60°C underscore the great promise. Stability at higher operating

temperatures must be improved, but even at its current state the PtNi nanorods are a eminent improvement over carbon supported Pt nanoparticles.

7.5 Appendix

The optimal annealing temperature, environment and time were found by systematically changing these parameters. The experiments concerning optimization of the annealing procedure were performed on a prior version to the catalyst described in the paper. This particular catalyst was a ternary PtNiFe catalyst, with the iron present from contamination in the sputtering targets. The morphology and surface area were identical to the PtNi catalyst describes in the paper. The activity for the oxygen reduction reaction (ORR) was about 25% lower for the PtNiFe catalyst as compared to the PtNi.

7.5.1 General observations during the annealing

When the temperature is ramped up, a red deposition is visible on the quartz tube when the temperature is increased above 300°C in H_2. This is residue of the perylene red, Inductively Coupled Photon Mass Spectroscopy (ICPMS) confirmed that no Pt, Ni or Fe was present in this residue. This confirms the removal of the red polymer substrate, without modifying the metal composition of the catalyst.

7.5.2 Effect of annealing temperature

The effect of annealing temperature and atmosphere can be seen in figure 7.7. Part A shows the cyclic voltammetry (CV) of those catalysts, and the main difference can be spotted in the H_{upd} region of the graph. Where the NSTF and the catalyst, annealed at 300°C in Argon show a peak at 0.1V vs RHE, the hydrogen annealed curves do not. Those hydrogen annealed catalysts have a broader H_{upd} region with a slight feature visible at about 0.2V. The OH_{ads} region is not obviously shifted more positive for the hydrogen annealed catalysts. The effect on the oxygen reduction reaction (ORR) activity is clear, however. Part B shows an optimum reached for annealing above 350°C. When the catalyst was annealed at even higher temperatures, the particles start agglomerating, and a successful transfer to the glassy carbon (GC) substrate was no longer able to be achieved.

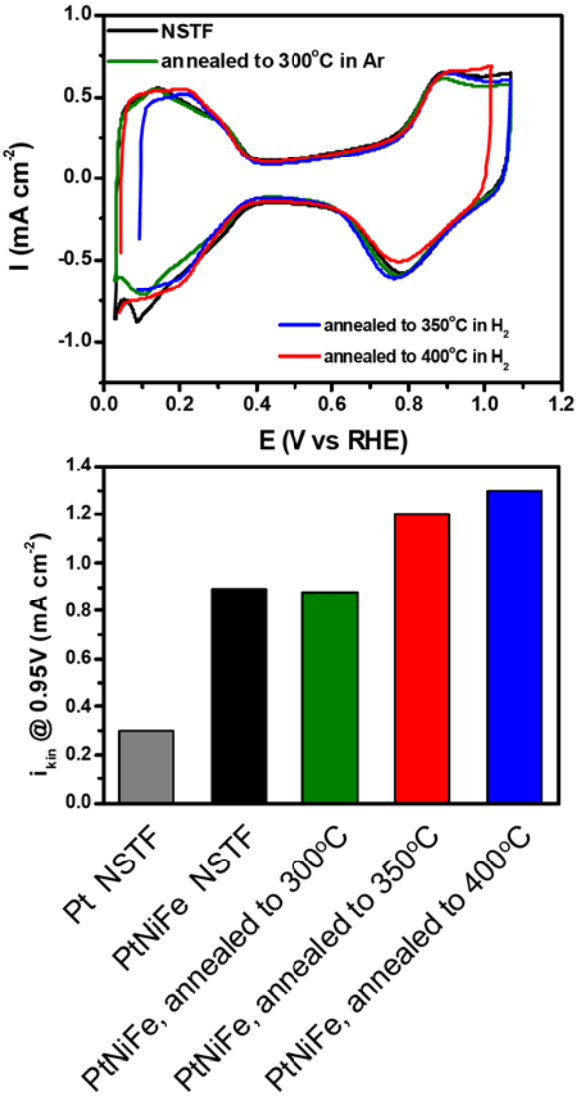

Figure 7.7. Effect of annealing temperature and atmosphere on blank cyclic voltammetry and oxygen reduction reaction. Black line in part A represents the PtNiFe NSTF catalyst, green, blue and red represent annealing at 300°C in Ar, 350°C in H_2 and 400°C in H_2, respectively. Scans were measured in 0.1 M $HClO_4$ at 50 mV s^{-1}.
Part B represents kinetic current density values, measured at 0.95 V vs RHE in the ORR curve in 0.1 M $HClO_4$ with 1600 rpm rotation and a scan rate of 20 mV s^{-1}. The grey bar represents monometallic Pt NSTF, the other colors represent the same catalysts as those in part A.

7.5.3 Different annealing environments

Figure 7.8 shows blank CVs obtained after annealing the particles in an alternate way. The red curve in the graph shows the annealing as described in the paper, with annealing for 4 hours in H_2, followed by cooling in Ar/H_2 overnight (annealing method 1). The blue curve represents an annealing method 2. In this method, the particles were annealed as described in method, but with a follow-up treatment of 15 minutes in which the particles were exposed to UV light in ozone. The goal was to remove any residual organics by oxidation after the surface was already annealed, to improve cleanliness. Finally, the orange curve shows annealing method 3, in which the particles were first annealed for 1 hour in pure oxygen to 300°C, to oxidize as many organics as possible, followed by a 3 hour annealing in H_2 to reduce surface oxides.

The effect on the CV is minimal. In the alternate annealing methods, the H_{upd} are is not as flat and (111)-like as in method 1, and OH adsorbtion has a slightly lower onset. The effect on the ORR activity is also minimal; the values are not shown as the catalysts exhibit identical kinetic activities within margin of error.

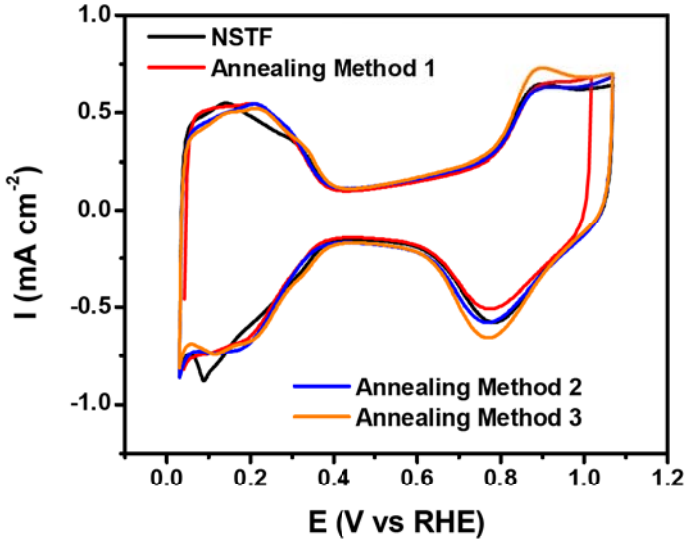

Figure 7.8. Effect of different annealing methods on the blank CV. Scans measured in 0.1 M $HClO_4$ with 50 mV s^{-1}. Black line represents the NSTF, the red, orange and blue lines represent annealing methods 1 through 3; for details see text.

7.5.4 Effect of annealing time

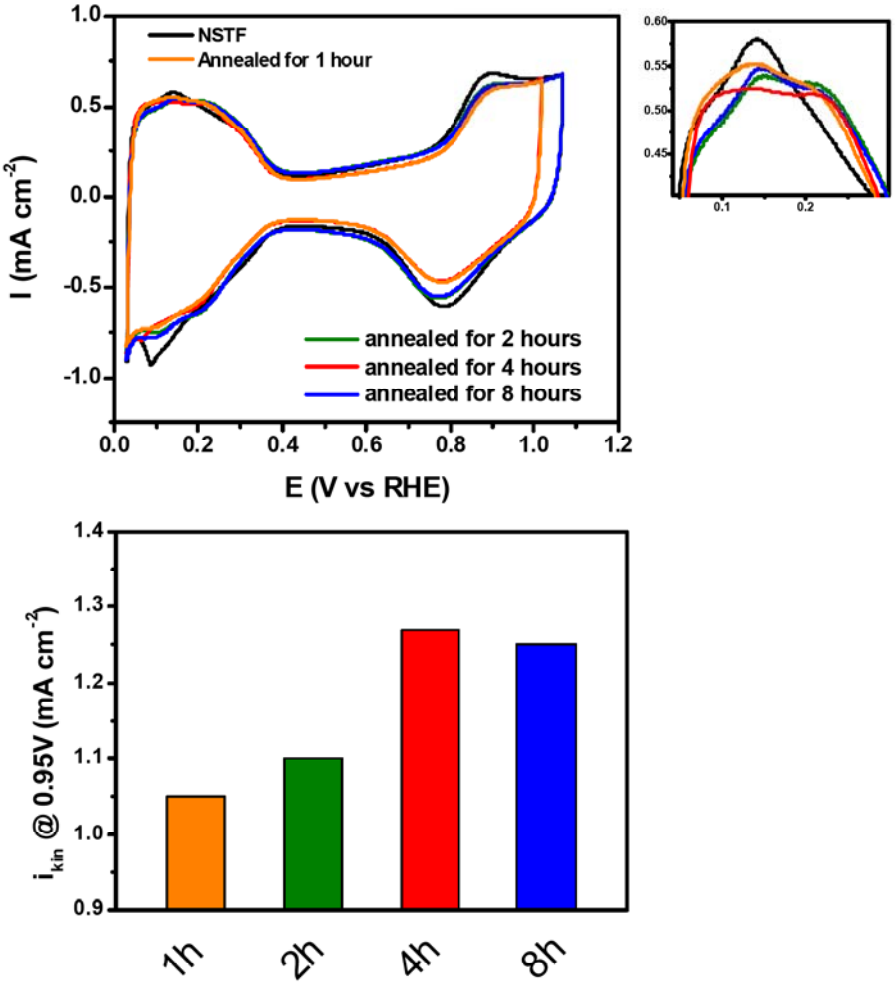

Figure 7.9. Effect of annealing time. Part A shows the blank cyclic voltammetries, with the inset a zoom in on the H_{upd} area of the curve. Black line represents the NSTF, orange, green, red and blue lines show the CVs for 1, 2, 4 and 8 hours annealing time, respectively.
Part B shows the effect on the kinetic current density for the ORR at 0.95V vs RHE, as measures in 0.1 M $HClO_4$ with 1600 rpm and 20 mV s^{-1}. Colors match those assigned in part A.

The duration of annealing was investigated as well. The particles were still gradually ramped up to a temperature of 400°C, but the duration they were kept at 400°C was varied. Blank CVs and ORR activities for these catalysts are shown in Figure 7.9. The zoom-in shows clearly the effect of annealing on the H_{upd} region of

the CV. The peak at 0.1 V, visible in the blank CV of PtNiFe NSTF is retained when the particles are only annealed for an hour, but the feature at 0.2V gets more pronounced with increasing annealing time. The onset of OH adsorbtion is identical in all catalysts. The apparent smaller double layer region (in between the H_{upd} and OH_{ads} regions) is due to the fact that the curves are showing current densities (normalized for surface area), where the double layer is geometrical surface area dependant. When the CVs are plotted showing the currents (non-normalized) then the double layers are equal in size and shape.

The ORR activities show a dependence on the annealing time. Up to 4 hours of annealing, the activity increases with increasing annealing time, and then remains essentially constant.

7.5.5 Effect on Active Surface Area

Figure 7.10 shows the active surface area in m^2 per gram catalyst used. It is assumed that the Pt content of the particles does not alter. This assumption is based on the fact that the Energy Dispersive X-ray (EDX) spectra of the catalyst after annealing (figure 7.11) shows the particles have the same composition within margins of error as before the annealing. Catalyst composition of the NSTF was supplied by 3M. The Pt content was 6% higher in the annealed particles, but that can be explained by the removal of the polymer substrate of the NSTF, see point 1 above.

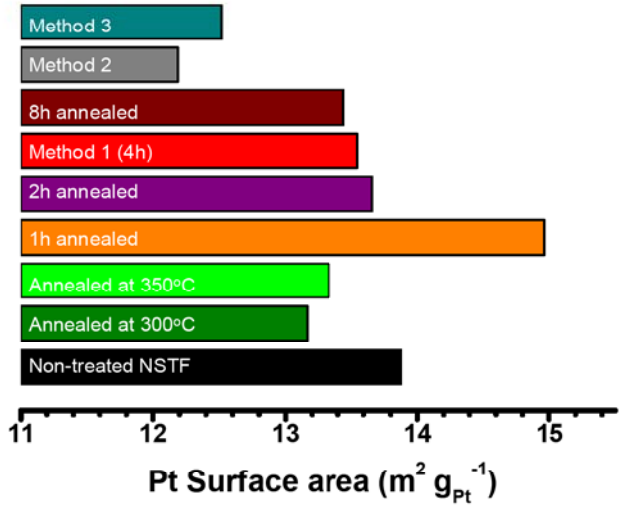

Figure 7.10. Effect of annealing treatment on the active surface area.

Shorter annealing times seem to give rise to a larger active surface area. This is because the removal of the polymer substrate is a faster process than the smoothening of the surface of the particles. Initially, the surface area is increased by making parts of the inside of the nanotubes available for catalytic reactions through removal of the perylene red; and at longer time scales the surface is slowly annealed and made smoother.

Because the kinetic activity for the ORR increases when the particles are smoother, the loss in surface area does not reflect in a loss of mass activity, on the contrary, mass activity is increased for the 4 hour annealed particles, compared to the 1 hour annealed catalyst, which in turn is more active per unit mass than the NSTF.

The alternative annealing methods show a decrease in active surface area. This is likely because part of the surface has oxidized irreversibly, and no longer shows activity towards hydrogen adsorption or ORR. This means that the mass activities are smaller than the particles annealed with Method 1.

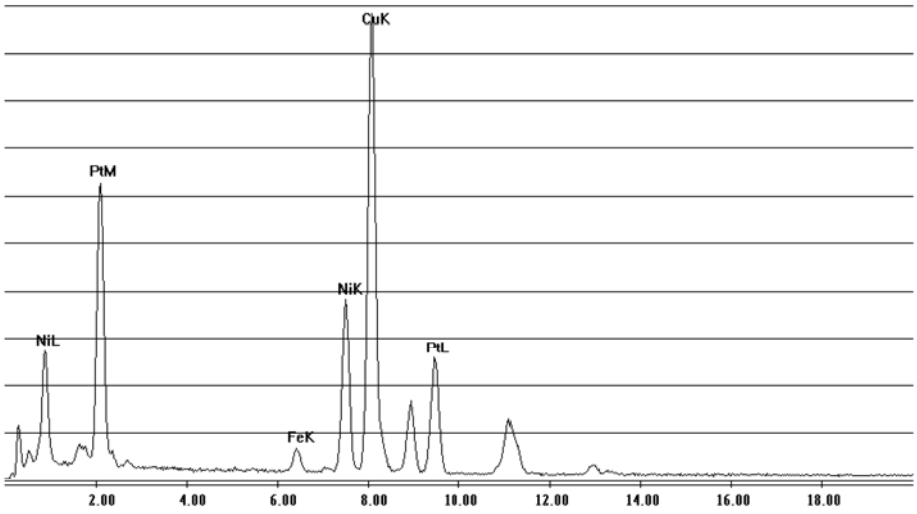

Figure 7.11. EDX spectrum of the 8 hour annealed particles.

References

[1] H. A. Gasteiger, S. S. Kocha, B. Sompalli, and F. T. Wagner, Applied Catalysis B-Environmental. 56 (2005) 9.

[2] H. A. Gasteiger, J. E. Panels, and S. G. Yan, Journal of Power Sources. 127 (2004) 162.

[3] K. J. J. Mayrhofer, B. B. Blizanac, M. Arenz, V. R. Stamenkovic, P. N. Ross, and N. M. Markovic, Journal of Physical Chemistry B. 109 (2005) 14433.

[4] J. X. Wang, N. M. Markovic, and R. R. Adzic, Journal of Physical Chemistry B. 108 (2004) 4127.
[5] L. Xiao, L. Zhuang, Y. Liu, J. T. Lu, and H. D. Abruna, Journal of the American Chemical Society. 131 (2009) 602.
[6] J. Hernandez, J. Solla-Gullon, E. Herrero, A. Aldaz, and J. M. Feliu, Journal of Physical Chemistry C. 111 (2007) 14078.
[7] L. G. R. A. Santos, K. S. Freitas, and E. A. Ticianelli, Electrochimica Acta. 54 (2009) 5246.
[8] A. S. Arico, P. Bruce, B. Scrosati, J. M. Tarascon, and W. Van Schalkwijk, Nature Materials. 4 (2005) 366.
[9] A. Atkinson, S. Barnett, R. J. Gorte, J. T. S. Irvine, A. J. Mcevoy, M. Mogensen, S. C. Singhal, and J. Vohs, Nature Materials. 3 (2004) 17.
[10] P. Strasser, S. Koh, T. Anniyev, J. Greeley, K. More, C. Yu, Z. Liu, S. Kaya, D. Nordlund, H. Ogasawar, M. F. Toney, and A. Nilsson, Nature Chemistry. Published online: 25 April 2010 | doi:10.1038/nchem.623 (2010).
[11] K. J. J. Mayrhofer and M. Arenz, Nature Chemistry. 1 (2009) 518.
[12] J. Greeley, I. E. L. Stephens, A. S. Bondarenko, T. P. Johansson, H. A. Hansen, T. F. Jaramillo, J. Rossmeisl, I. Chorkendorff, and J. K. Norskov, Nature Chemistry. 1 (2009) 552.
[13] D. Strmcnik, K. Kodama, D. van der Vliet, J. Greeley, V. R. Stamenkovic, and N. M. Markovic, Nature Chemistry. 1 (2009) 466.
[14] S. Gupta, D. Tryk, I. Bae, W. Aldred, and E. Yeager, Journal of Applied Electrochemistry. 19 (1989) 19.
[15] S. L. Gupta, D. Tryk, W. Aldred, I. T. Bae, and E. Yeager, Journal of the Electrochemical Society. 134 (1987) C129.
[16] M. Lefevre, E. Proietti, F. Jaouen, and J. P. Dodelet, Science. 324 (2009) 71.
[17] F. Jaouen, J. Herranz, M. Lefevre, J. P. Dodelet, U. I. Kramm, I. Herrmann, P. Bogdanoff, J. Maruyama, T. Nagaoka, A. Garsuch, J. R. Dahn, T. Olson, S. Pylypenko, P. Atanassov, and E. A. Ustinov, Acs Applied Materials & Interfaces. 1 (2009) 1623.
[18] R. Kothandaraman, V. Nallathambi, K. Artyushkova, and S. C. Barton, Applied Catalysis B-Environmental. 92 (2009) 209.
[19] K. Kendall, Nature Materials. 1 (2002) 211.
[20] V. R. Stamenkovic, B. Fowler, B. S. Mun, G. F. Wang, P. N. Ross, C. A. Lucas, and N. M. Markovic, Science. 315 (2007) 493.
[21] V. Stamenkovic, T. J. Schmidt, P. N. Ross, and N. M. Markovic, Journal of Physical Chemistry B. 106 (2002) 11970.
[22] V. R. Stamenkovic, B. S. Mun, K. J. J. Mayrhofer, P. N. Ross, and N. M. Markovic, Journal of the American Chemical Society. 128 (2006) 8813.
[23] M. R. Miah and T. Ohsaka, Electrochimica Acta. 54 (2009) 5871.
[24] F. Tian and A. B. Anderson, Journal of Physical Chemistry C. 112 (2008) 18566.
[25] S. Koh and P. Strasser, Journal of the American Chemical Society. 129 (2007) 12624.
[26] M. H. Shao, T. Huang, P. Liu, J. Zhang, K. Sasaki, M. B. Vukmirovic, and R. R. Adzic, Langmuir. 22 (2006) 10409.
[27] V. R. Stamenkovic, B. S. Mun, M. Arenz, K. J. J. Mayrhofer, C. A. Lucas, G. F. Wang, P. N. Ross, and N. M. Markovic, Nature Materials. 6 (2007) 241.
[28] J. L. Zhang, M. B. Vukmirovic, Y. Xu, M. Mavrikakis, and R. R. Adzic, Angewandte Chemie-International Edition. 44 (2005) 2132.

[29] S. Mukerjee and S. Srinivasan, Journal of Electroanalytical Chemistry. 357 (1993) 201.
[30] U. A. Paulus, A. Wokaun, G. G. Scherer, T. J. Schmidt, V. Stamenkovic, N. M. Markovic, and P. N. Ross, Electrochimica Acta. 47 (2002) 3787.
[31] U. A. Paulus, A. Wokaun, G. G. Scherer, T. J. Schmidt, V. Stamenkovic, V. Radmilovic, N. M. Markovic, and P. N. Ross, Journal of Physical Chemistry B. 106 (2002) 4181.
[32] T. Toda, H. Igarashi, H. Uchida, and M. Watanabe, Journal of the Electrochemical Society. 146 (1999) 3750.
[33] F. J. Lai, L. S. Sarma, H. L. Chou, D. G. Liu, C. A. Hsieh, J. F. Lee, and B. J. Hwang, Journal of Physical Chemistry C. 113 (2009) 12674.
[34] P. Mani, R. Srivastava, and P. Strasser, Journal of Physical Chemistry C. 112 (2008) 2770.
[35] Y. Tamura, K. Taneda, M. Ueda, and T. Ohtsuka, Corrosion Science. 51 (2009) 1560.
[36] F. H. B. Lima, J. F. R. de Castro, L. G. R. A. Santos, and E. A. Ticianelli, Journal of Power Sources. 190 (2009) 293.
[37] K. J. J. Mayrhofer, D. Strmcnik, B. B. Blizanac, V. Stamenkovic, M. Arenz, and N. M. Markovic, Electrochimica Acta. 53 (2008) 3181.
[38] S. Mukerjee, S. Srinivasan, M. P. Soriaga, and J. Mcbreen, Journal of the Electrochemical Society. 142 (1995) 1409.
[39] S. Mukerjee, S. Srinivasan, M. P. Soriaga, and J. Mcbreen, Journal of Physical Chemistry. 99 (1995) 4577.
[40] L. Gancs, T. Kobayashi, M. K. Debe, R. Atanasoski, and A. Wieckowski, Chemistry of Materials. 20 (2008) 2444.
[41] T. J. Schmidt, H. A. Gasteiger, G. D. Stab, P. M. Urban, D. M. Kolb, and R. J. Behm, Journal of the Electrochemical Society. 145 (1998) 2354.
[42] A. J. Bard and L. R. Faulkner, Electrochemical Methods, J. Wiley & Sons, New York, 1980.
[43] V. Stamenkovic, T. J. Schmidt, P. N. Ross, and N. M. Markovic, Journal of Electroanalytical Chemistry. 554 (2003) 191.
[44] D. S. Strmcnik, D. V. Tripkovic, D. van der Vliet, K. C. Chang, V. Komanicky, H. You, G. Karapetrov, J. Greeley, V. R. Stamenkovic, and N. M. Markovic, Journal of the American Chemical Society. 130 (2008) 15332.
[45] M. K. Debe and A. R. Drube, Journal of Vacuum Science & Technology B. 13 (1995) 1236.
[46] M. K. Debe and R. J. Poirier, Journal of Vacuum Science & Technology a-Vacuum Surfaces and Films. 12 (1994) 2017.
[47] M. K. Debe, A. K. Schmoeckel, G. D. Vernstorn, R. Atanasoski, Journal of Power Sources. 161 (2006) 1002.
[48] J.C. Serrano-Ruiz, A. López-Cudero, J. Solla-Gullón, A. Sepúlveda-Escribano, A. Aldaz and F. Rodríguez-Reinoso, Journal of Catalysis. 253 (2008) 159.
[49] N. M. Markovic and P. N. Ross, Surface Science Reports. 45 (2002) 117.